

# **Axon diameters and myelin content modulate microscopic fractional anisotropy at short diffusion times in fixed rat spinal cord**

Noam Shemesh

Champalimaud Neuroscience Programme, Champalimaud Centre for the Unknown, Lisbon,  
Portugal

\*Corresponding author:

Dr. Noam Shemesh, Champalimaud Neuroscience Programme, Champalimaud Centre for the Unknown, Av. Brasilia 1400-038, Lisbon, Portugal

E-mail: [noam.shemesh@neuro.fchampalimaud.org](mailto:noam.shemesh@neuro.fchampalimaud.org);

Phone number: +351 210 480 000 ext. #4467

Running title: Microstructural correlates of microscopic anisotropy

Figures: 8

Tables: 3

## Abstract

Mapping tissue microstructure accurately and noninvasively is one of the frontiers of biomedical imaging. Diffusion Magnetic Resonance Imaging (MRI) is at the forefront of such efforts, as it is capable of reporting on microscopic structures orders of magnitude smaller than the voxel size by probing restricted diffusion. Double Diffusion Encoding (DDE) and Double Oscillating Diffusion Encoding (DODE) in particular, are highly promising for their ability to report on microscopic fractional anisotropy ( $\mu$ FA), a measure of the pore anisotropy in its own eigenframe, irrespective of orientation distribution. However, the underlying correlates of  $\mu$ FA have insofar not been studied. Here, we extract  $\mu$ FA from DDE and DODE measurements at ultrahigh magnetic field of 16.4T in the aim to probe fixed rat spinal cord microstructure. We further endeavor to correlate  $\mu$ FA with Myelin Water Fraction (MWF) derived from multiexponential  $T_2$  relaxometry, as well as with literature-based spatially varying axonal diameters. In addition, a simple new method is presented for extracting unbiased  $\mu$ FA from three measurements at different b-values. Our findings reveal strong anticorrelations between  $\mu$ FA (derived from DODE) and axon diameter in the distinct spinal cord tracts; a moderate correlation was also observed between  $\mu$ FA derived from DODE and MWF. These findings suggest that axonal membranes strongly modulate  $\mu$ FA, which – owing to its robustness towards orientation dispersion effects – reflects axon diameter much better than its typical FA counterpart. The  $\mu$ FA exhibited modulations when measured via oscillating or blocked gradients, suggesting selective probing of different parallel path lengths and providing insight into how those modulate  $\mu$ FA metrics. Our findings thus shed light into the underlying microstructural correlates of  $\mu$ FA and are promising for future interpretations of this metric in health and disease.

**Keywords:** Microscopic Anisotropy, MRI, microstructure, diffusion MRI, myelin water fraction, spinal cord, axon diameter

## Introduction

Diffusion Magnetic Resonance Imaging (MRI) has become a mainstay of contemporary microstructural imaging in biomedical applications. Diffusion MRI can provide rich information on the sample's microstructure by interrogating micron-scale dimensions within millimeter-scale voxels (Johansen-Berg, H, Behrens, 2009). In the hierarchical scaling of dimensions in biological systems, the micron-scale is fortuitously a characteristic length scale of many (sub)cellular structures of interest, such as axons, dendrites or cell bodies, which cannot be accessed using routine spatial resolutions in MRI. Most diffusion MRI methods utilize variants of Stejskal and Tanner's (Stejskal, E.O., Tanner, 1965) Single Diffusion Encoding (SDE) technique (Shemesh et al., 2016), which probes diffusion using a single diffusion epoch spanned by diffusion-sensitizing gradient waveforms. The flexibility of SDE in terms of parameter space led to numerous variants (Grebenkov, 2007), as well as diffusion models (Assaf et al., 2013; Panagiotaki et al., 2012), that have been devised to probe different aspects of the microstructure. For example, Diffusion Tensor Imaging (DTI) models diffusion using a single tensor (Basser and Jones, 2002; Mori and Zhang, 2006) under the assumption of (time-dependent) Gaussian diffusion, and the tensor's rotationally invariant properties can then report on diffusion anisotropy and parallel/perpendicular diffusivities. Other methods, such as q-space imaging (Callaghan et al., 1991; Cohen and Assaf, 2002) or diffusion spectrum imaging (Wedeen et al., 2005) utilize Fourier relationships between the diffusion propagator and signal decay with the q-value (where  $\mathbf{q} = \frac{1}{2\pi}\gamma\delta\mathbf{G}$  is the wavevector,  $\gamma$  is the gyromagnetic ratio,  $\delta$  represents the gradient duration, and  $|\mathbf{G}|$  is the gradient amplitude) to extract information on pore size or orientation distributions, respectively. Diffusion time- and/or frequency-dependence can also provide much insight into the restricting geometry by probing the way in which the diffusion path is modulated with time and/or the diffusion spectrum, respectively (Clark et al., 2001; Fieremans et al., 2016; Gore et al., 2010; Jespersen et al., 2017a; Latour et al., 1994; Novikov et al., 2011; Stepišnik et al., 2006; Veraart et al., 2016a). Furthermore, more advanced biophysical modeling has been recently put forth to characterize specific microstructural components such as neurite density (Jespersen et al., 2007, 2010), or water fractions tentatively associated with axons in white matter (Veraart et al., 2016a) from specific acquisition schemes. Such SDE methods have been widely useful in neuroscience (Zatorre et al., 2012) and biomedical applications, typically targeting longitudinal processes such as stroke, learning, or chronic disease progression (Johansen-Berg, H, Behrens, 2009).

One interesting metric that can be probed by diffusion is the microscopic diffusion anisotropy ( $\mu A$ ) (Callaghan and Komlosh, 2002; Cheng and Cory, 1999; Mitra, 1995), from which its normalized counterpart – the microscopic fractional anisotropy ( $\mu FA$ ) – can be derived.  $\mu FA$  defines a single compartment's anisotropy in its own eigenframe (Jespersen et al., 2013), e.g., for a sphere  $\mu FA = 0$  while for an infinite cylinder  $\mu FA$  can approach 1. However, in practice, the MRI signal will always originate from an ensemble, thereby making it necessary to account for orientation dispersion within the ensemble (Jespersen et al., 2017c). In systems comprising coherently-aligned anisotropic objects where orientation dispersion is ideally zero,  $\mu FA$  would be equivalent to the fractional anisotropy (FA) derived from DTI. However, in conventional SDE methods, when orientation dispersion is significant, estimated FA values typically do not represent the true anisotropy, or  $\mu FA$ , as they are conflated with orientation dispersion (Mollink et al., 2017; Reisert et al., 2017). For example, in ideal randomly oriented infinite cylinders, the averaging of

anisotropic compartments results in  $FA = 0$ , which – without a-priori knowledge or extensive modelling – would suggest that the microscopic geometry is spherical.

In recent years, the Double Diffusion Encoding (DDE) methodology (Figure 1) has been gaining increasing attention for its potential to refine and identify microstructural aspects not so easily probed by SDE (Cory, DG, Garroway, AN, Miller, 1990; Mitra, 1995). Unlike SDE, DDE probes diffusion correlations using – as its name suggests – two diffusion encoding periods, spanned by two independent gradient wavevectors, which are separated by a mixing time ( $\tau_m$ ). Comparing q-space-like signal decays using parallel and perpendicular relative gradient orientations, Cheng and Cory have been able to measure the sizes of randomly oriented elongated (anisotropic) yeast cells, and distinguish them from spherical cells (Cheng and Cory, 1999). Similarly, Callaghan and Komlosh have shown that diffusivities extracted from parallel vs. perpendicular DDE could provide insight into  $\mu FA$  in randomly oriented liquid crystals characterized by Gaussian diffusion (Callaghan and Komlosh, 2002). Such measurements provided the first clues that  $\mu FA$  (termed using many divergent terms (Shemesh et al., 2016)) could be recovered from DDE irrespective of orientation dispersion.

Mitra (Mitra, 1995), and later Özarlsan (Özarlsan, 2009) derived exact solutions for DDE signals, and have identified the importance of the mixing time in decoupling  $\mu A$  from other effects. In the short mixing time regime, interesting diffusion-diffraction phenomena can be produced (Laun et al., 2011, 2012, Shemesh et al., 2010a, 2010b, 2012b), and angular dependencies can provide insight into pore sizes as shown experimentally first by Koch and Finsterbusch (Koch and Finsterbusch, 2008, 2011) and then by others (Komlosh et al., 2011; Morozov et al., 2015; Shemesh et al., 2009); however, by analyzing the displacement correlation tensor (Nørhøj Jespersen and Buhl, 2011), the short  $\tau_m$  angular DDE experiment was found by Jespersen to be equivalent to a time-dependent SDE experiment (Jespersen, 2012). By contrast, in the long mixing time regime,  $\mu A$  is decoupled from these restriction effects, making its measurement much less complicated (Mitra, 1995; Özarlsan, 2009). The ability to measure accurate  $\mu A$  values was validated in (Shemesh et al., 2010a) and its importance was shown in biological systems such as ex-vivo neural tissues (Shemesh and Cohen, 2011a), yeast cells (Shemesh et al., 2011), and preclinical in-vivo experiments (Shemesh et al., 2012a), where the orientational variance of the measurements was highlighted. Lawrenz et al have proposed rotationally invariant schemes for mapping an index of  $\mu A$  (Lawrenz et al., 2010; Lawrenz and Finsterbusch, 2015), and Jespersen et al subsequently generalized rotationally invariant DDE measurements up to 5<sup>th</sup> order (in q-values) via a measurement scheme termed DDE 5-design (Jespersen et al., 2013). Numerous promising studies have also been performed on human scanners (Avram et al., 2013; Finsterbusch, 2011; Koch and Finsterbusch, 2008, 2011; Lawrenz and Finsterbusch, 2015; Ulloa et al., 2015), suggesting quite promising potential for disentangling  $\mu FA$  from the underlying orientation dispersion. Additional recent experiments have even extended the DDE methodology towards MR spectroscopy, aiming to impart specificity towards specific cell populations via cellular-specific metabolites (Shemesh et al., 2014a, 2017).

As alluded to above, the diffusion process in biological tissues is highly time-dependent, and thus the filter with which the diffusion experiment is performed can be important. Oscillating Diffusion Encoding (ODE) experiments (Does et al., 2003; Gore et al., 2010; Stepišnik, 1993) have been widely used in SDE to enhance contrast in neural tissue, likely since they access shorter diffusion time than could be reached using pulsed-gradient-spin-echo methods (Drobnjak et al., 2016).

Additionally, ODE has been shown to be highly beneficial for mapping axonal sizes in rat spinal cord (Xu et al., 2009, 2014) as well as for contrasting malignancy in tissues (Reynaud et al., 2016; Xu et al., 2012). More recently, the DDE framework was extended towards accommodation of oscillating gradients, termed Double Oscillating Diffusion Encoding (DODE, Figure 1A), first in theory (Ianuş et al., 2017b), and more recently, in experiment (Ianuş et al., 2017a). Importantly, DODE enables the time/frequency-dependence of  $\mu$ FA to be studied. Furthermore, DODE sequences reach the long mixing time regimes much more easily than their DDE counterparts, thereby making the experiments less mixing-time dependent (Ianuş et al., 2017b), and, as a result, offering the benefit of reduced echo times. This property is likely due to the mixing beginning already from the first gradient pair, and accumulating over the entire gradient waveform. Such DODE experiments were recently reported for the first time in the ex-vivo mouse brain, and  $\mu$ FA maps derived from DODE indeed showed richer contrast than those of their DDE-derived counterparts (Ianuş et al., 2017a).

Many studies have investigated the underlying microstructural correlates of FA, mainly in white matter (for a classical review, the reader is referred to (Beaulieu, 2002)). It is clear that although myelin strongly modulates FA, it is not necessary for detection of anisotropy in biological systems. Axonal membranes, for example, can impede the diffusion processes with orientational preference and thus can contribute to FA. However, in most studies attempting to investigate the origins of restriction in tissues, orientation dispersion was conflated with SDE-driven metrics; an interesting question is therefore whether  $\mu$ FA, which should not suffer from orientation dispersion effects, could be associated with microstructural features to different extents than FA. *The goal of this study was therefore to investigate how  $\mu$ FA and FA correlate underlying microstructural features such as myelin water fraction (MWF) or axonal diameters.* As well, we aimed to investigate whether these parameters are differently correlated, to qualitatively assess the importance of orientation dispersion, especially in the white matter. The final goal of this study was to determine whether  $\mu$ FA is modulated when different length scales are probed via DODE and DDE sequences. A well-characterized system, namely, fixed spinal cord – which has been extensively used in the past to study diffusion (Jespersen et al., 2017b; Klawiter et al., 2011; Komlosh et al., 2008; Schwartz et al., 2005; Xu et al., 2014) or relaxation (Kozlowski et al., 2008a, 2008b; Nunes et al., 2017; Wilhelm et al., 2012) microstructural correlates – was used for these investigations. Our findings demonstrate interesting differences in correlations between  $\mu$ FA and FA and MWF, as well as with the a-priori known axonal sizes in white matter, when measured using DODE or DDE. Interesting findings in gray matter tissues are also presented. Implications for D(O)DE contrasts and future routes for investigations of the origin of  $\mu$ FA in neural tissue, are discussed.

## Theory

Most MRI studies up to date have used only a single b-value to extract  $\mu\text{FA}$  from DDE experiments. However, very recently, Ianus et al showed that for most plausible microstructural scenarios,  $\mu\text{FA}$  obtained in such a way can be highly biased due to neglecting the higher-order terms in the signal decay (Ianus et al., 2017a). Ianus et al proposed to more accurately estimate  $\mu\text{FA}$  in both DDE and DODE methodologies by performing D(O)DE experiments at multiple b-values, and fitting both  $\mu\text{A}$  (from which  $\mu\text{FA}$  is then calculated) and the higher-order term via polynomial fits. That is, the D(O)DE signal decay at long mixing times can be expanded with b-value as:

[Eq. 1]

$$\frac{1}{12} \sum \log(S_{\parallel}(b)) - \frac{1}{60} \sum \log(S_{\perp}(b)) = \mu A^2 b^2 + P_3 b^3,$$

where  $\mu A^2 = \frac{3}{5} \text{var}(\sigma_i)$ ,  $\sigma_{i=1,2,3}$  are the diffusion tensor eigenvalues,  $S_{\parallel}$  and  $S_{\perp}$  represent the D(O)DE signals acquired using parallel and perpendicular gradients, respectively, and  $P_3$  contains the higher-order terms. Ianus et al showed that polynomial fitting can be used to estimate  $\mu A^2$  and  $P_3$  from Eq. 1. When the mean diffusivity (MD) is additionally measured at lower b-values (e.g., from fitting a tensor to the 12 parallel orientations in the 5-design),  $\mu\text{FA}$  can be directly calculated from Eq. 2:

[Eq. 2]

$$\mu\text{FA} = \sqrt{\frac{3}{2} \frac{\mu A^2}{\mu A^2 + \frac{3}{5} \text{MD}^2}}.$$

Although polynomial fitting probably yields the more accurate estimates of  $\mu A^2$ , it should be noted that ideally, many b-value shells would be required for robust fitting. An alternative approach would be to acquire a much more minimalistic dataset and still be able to quantify  $\mu A^2$  and  $P_3$ . Setting  $\frac{1}{12} \sum \log(S_{\parallel}(b)) - \frac{1}{60} \sum \log(S_{\perp}(b)) \equiv \tilde{\epsilon}(b)$ , Eq. 1 can be rewritten for two different b-values  $b_1$  and  $b_2$ :

[Eq. 3]

$$\begin{cases} \tilde{\epsilon}(b_1) = \mu A^2 b_1^2 + P_3 b_1^3 \\ \tilde{\epsilon}(b_2) = \mu A^2 b_2^2 + P_3 b_2^3 \end{cases}$$

It is then straightforward to show that from two measurements at different b-values,  $\mu A^2$  can be directly obtained from

[Eq. 4]

$$\widetilde{\mu A^2} = \frac{\tilde{\epsilon}(b_2) - \tilde{\epsilon}(b_1) \frac{b_2^3}{b_1^3}}{b_2^2 - \frac{b_2^3}{b_1}},$$

which can then be plugged into Eq. 2 to obtain  $\mu$ FA directly. Note that we use the tilde to distinguish the extracted  $\widetilde{\mu A^2}$  from the real  $\mu A^2$ . This approach for accurate  $\mu$ FA extraction thus requires, in principle, only two measurements, one at low b-value, from which MD and  $\tilde{\epsilon}(b_1)$  would be obtained, and another at higher b-value, where  $\tilde{\epsilon}(b_2)$  would be obtained. However, since at low b-values required for accurate estimation of MD,  $\tilde{\epsilon}(b_1)$  may be very small and comparable to noise levels, it is more appropriate to acquire  $\tilde{\epsilon}(b_1)$  and  $\tilde{\epsilon}(b_2)$  at somewhat higher b-values (where the  $b^2$  terms are more dominant) and perform a separate, third acquisition for extracting MD at lower b-values. This 3-shell approach was thus preferred in this study.

## Materials and Methods

This study was carried out in accordance with the recommendations of the directive 2010/63/EU of the European Parliament of the Council, authorized by the Champalimaud Centre for the Unknown's Animal Welfare Body, and approved by the national competent authority (Direcção Geral de Alimentação e Veterinária, DGAV).

**Specimen Preparation.** Spinal cord specimens were obtained from adult male Wistar rats (N=2) weighing ~300 gr. The rats underwent standard transcardial perfusion under deep pentobarbital anesthesia. Cervical spinal cords were extracted, washed in PBS, and kept in 4% paraformaldehyde (PFA) for 24h at 4°C. The samples were then placed in freshly prepared phosphate buffer saline (PBS) for at least 48h prior to MRI experiments. The samples were cut to ~1cm lengths and placed in a 5 mm NMR tube filled with fluorinert (Sigma Aldrich, Lisbon, Pt).

**MRI experiments.** All MRI experiments were performed on a vertical 16.4T (700 MHz  $^1\text{H}$  frequency) Aeon Ascend scanner (Bruker, Karlsruhe, Germany) interfaced with a Bruker AVANCE IIIHD console. A Micro5 probe equipped with a 5 mm birdcage coil for transmit and receive functions and a gradient system capable of producing amplitudes of up to 3T/m isotropically was used. The sample was kept at a constant temperature of 23 °C throughout the experiments by means of air flow, and the samples were allowed to equilibrate with the surrounding temperature for at least 4 h before acquiring any diffusion or relaxation experiments.

All diffusion sequences were written in-house and were based on an Echo Planar Imaging (EPI) readout. For both DODE and DDE, the same acquisition parameters were used, namely, two-shot and double-sampled EPI with a readout bandwidth of 555.555 kHz, Field of View (FOV) of 6x4 mm<sup>2</sup> and in-plane matrix size of 120x80, leading to an isotropic in-plane resolution of 50x50  $\mu\text{m}^2$ . The slice thickness was 500  $\mu\text{m}$ , and TR/TE = 2500/52 ms. For both DODE and DDE acquisitions, Jespersen's 5-design sampling scheme (Jespersen et al., 2013) was used for the diffusion weighted images, and, additionally, eight images with zero b-value were acquired, such that the total number of images acquired in a given scan was 80. For both DODE and DDE, three separate acquisitions were performed with different b-values, namely,  $2b = 1.2, 2.4$  and  $3.0 \text{ ms}/\mu\text{m}^2$  (where the factor of 2 reflects the accumulated diffusion weighting along the two diffusion epochs). The specific b-values were chosen based on signal-to-noise and contrast considerations: on the one hand, they have to be sufficiently low such that even higher-order terms do not contribute, but on the other hand, they have to be high enough for  $\mu\text{FA}$  contrast to be detectable. The lowest b-value scans were acquired with 12 averages, while the other two b-value shells were acquired with 32 averages each. The DODE diffusion parameters were:  $T_{\text{DODE}} = 13 \text{ ms}$ ,  $N = 5$ ,  $\tau_s = 2 \text{ ms}$ . The DDE diffusion parameters were  $\Delta/\delta = 12/1 \text{ ms}$ ,  $\tau_m = 12 \text{ ms}$ , see Figure 1 for definitions of the parameters.

Additional experiments were performed for mapping myelin water fraction. Those consisted of a Carr-Purcell-Meiboom-Gill (CPMG)-based acquisition performed using a modified pulse multi-slice-multi-echo (MSME) sequence. The same slice was acquired as in the diffusion images with identical in-plane resolution and FOV. The acquisition bandwidth for the pulse sequence was 100 kHz, and the pulses used for slice-selective excitation and refocusing had durations of 1.16 ms (Shinnar-Le-Roux shape) and 50  $\mu\text{s}$  (Gaussian shape), respectively. The respective bandwidths of the excitation and refocusing pulses were 3625 Hz and 32100 Hz, respectively, such that the refocusing pulse provided complete refocusing on the entire slice. The  $\Delta\text{TE}$  that could be achieved



using these parameters was 2.85 ms, and 96 echoes were acquired from 2.85 to 273.6 ms. The repetition time was 2500 ms and two averages were acquired.

**Diffusion data preprocessing.** All preprocessing and analyses were performed using MatLab® (The MathWorks, Inc., Natick, Massachusetts, United States). Raw images were registered using an implementation of (Guizar-Sicairos et al., 2008) found in <https://goo.gl/3bGU8b>. The images were then denoised using Veraart’s algorithm based on Marchenko-Pastur distributions in Principal Component Analysis of redundant data (Veraart et al., 2016b). Gibbs unringing was performed using Kellner’s method (Kellner et al., 2016) implemented in Matlab . Finally, the denoised and unringed images were very slightly smoothed using a [2 2] median filter.

**Relaxation data preprocessing.** The preprocessing steps for the relaxation data were identical to the diffusion data preprocessing steps, except for an additional step in the very beginning of the pipeline whereby the magnitude data was converted to real data using Eichner’s method (Eichner et al., 2015). All steps listed above including denoising, unringing and median filter smoothing were then executed in sequence.

**Diffusion data analysis.** The first analysis step for D(O)DE data was to fit the diffusion tensor. Diffusivities were computed using a simple linear fitting of  $S_{||}$  data acquired at the lowest b-value experiments followed by diagonalization and extraction of the diffusion tensor eigenvalues. The mean diffusivity and fractional anisotropy were then calculated from the tensor eigenvalues as

$MD = \frac{1}{3}(\lambda_1 + \lambda_2 + \lambda_3)$  and  $FA = \sqrt{\frac{3}{2} \frac{(\lambda_1 - MD)^2 + (\lambda_2 - MD)^2 + (\lambda_3 - MD)^2}{\lambda_1^2 + \lambda_2^2 + \lambda_3^2}}$ , where  $\lambda_i$  represent the tensor eigenvalues.

The second step in the analysis was to use the data from the two higher b-values to extract  $\mu FA$ . First,  $\widetilde{\mu A^2}$  was extracted directly from Eq. 4; the mean diffusivity estimate was then used along with the extracted  $\widetilde{\mu A^2}$  to obtain  $\mu FA$  via Eq. 2.

**Relaxation data analysis.** Following the preprocessing steps listed above, the filtered relaxation data were subject to a voxelwise inverse Laplace Transform (iLT) using 150  $T_2$  components log-spaced between 2.1 and 328.3 ms. The  $T_2$  spectra were smoothed by minimum-curvature constraint as in (Dula et al., 2010) and extended phase graph analysis was performed to account for any  $B_1^+$  inhomogeneity and ensuing stimulated echoes (Prasloski et al., 2012). The myelin water fraction (MWF) was computed from each spectrum as the fraction of signal originating from components with peak  $T_2$  smaller than 17 ms. ROIs were drawn manually on the raw data closely following (Dula et al., 2010), and the ROI data was subjected to the same analysis using the mean signal decay in each ROI.

**Statistical analysis.** Gray matter and white matter masks were created by thresholding MWF maps with  $MWF < 0.22$  for gray matter and  $MWF > 0.25$  for white matter. The histograms in Figure 4 were then generated for each metric/method using Matlab’s *histogram* function which automatically selects the bin width to represent the underlying distribution in the most accurate way. Parameter means and standard deviations are reported in the text and Tables.

Correlation analyses between different diffusion metrics were performed using automatic outlier rejection (Grubbs test for outliers) followed by calculation of Spearman’s  $\rho$  ( $\mu FA$  and FA data

from all methods were not normally distributed). An analysis of variance (ANOVA) was performed to compare  $\mu$ FA and FA arising from DODE and DDE methods, with post-hoc Bonferroni tests corrected for multiple comparisons.

To correlate MWF with  $\mu$ FA or FA extracted from the different methods, the diffusion maps were registered to the MWF using Matlab's *imregister* function using a *multimodal* configuration, initial radius of  $1e-5$ , maximum number of iterations = 1000, and allowing for affine transformations due to the small differences in image geometry arising from EPI-based (diffusion) and line-by-line (relaxation) acquisitions.

When linear fits are presented (Figure 8), Matlab's *robustfit* function was used to extract the coefficients.

## Results

Diffusion data quality can be appraised in Figure 2, which plots representative raw data from one of the spinal cords, obtained from experiments with zero b-value (Fig. 2A), parallel (Fig. 2B), and perpendicular (Fig. 2C) diffusion orientations at the highest b-value used in this study. Before denoising, the worst-case signal to noise ratio (SNR) – measured at the highest b-value and with significant diffusion weighting gradients in the direction parallel to the spinal cord’s principal axis – was  $\sim 20$  in white matter. The middle column in Figure 2 shows the corresponding preprocessed data and the ensuing enhancement of image quality from denoising and Gibbs unringing (Figs 2D-F). Figures 2G-I show the result of subtracting raw and denoised images. The lack of structure in the subtracted images suggest that indeed only noise was removed and that no significant signal components were lost during denoising (Veraart et al., 2016b). The SNR of the preprocessed images was enhanced by a factor of  $\sim 2$ .

To assess the different maps obtained in this study, representative  $\mu$ FA and FA maps derived from DODE as well as DDE experiments (hereafter referred to as  $\mu$ FA<sub>DODE</sub> and  $\mu$ FA<sub>DDE</sub> or FA<sub>DODE</sub> and FA<sub>DDE</sub>, respectively) are shown in Figure 3. Several interesting qualitative features can be highlighted from these images: (1) both  $\mu$ FA<sub>DODE</sub> and  $\mu$ FA<sub>DDE</sub> maps (Figs. 3A and 3C) have higher values than their FA<sub>DODE</sub> and FA<sub>DDE</sub> counterparts (Figs. 3B and 3D) in white matter, as well as in gray matter; (2)  $\mu$ FA<sub>DDE</sub> is higher and less tract-specific when compared with  $\mu$ FA<sub>DODE</sub> (for approximate definitions of tract locations and spinal cord anatomy, the reader is referred to Figure 3E); (3)  $\mu$ FA<sub>DDE</sub> appears quite homogeneous in the WM while  $\mu$ FA<sub>DODE</sub> shows more variation within WM; (4) similarly, FA<sub>DDE</sub> is more homogeneous in white matter compared with FA<sub>DODE</sub>, which shows a greater variance in different tracts. To provide a more quantitative view on these features, Figure 4 plots histograms of  $\mu$ FA and FA in white matter and gray matter (c.f. Figure 4A and 4B for the ROI masks). In white matter,  $\mu$ FA<sub>DODE</sub> is higher than its FA<sub>DODE</sub> counterpart (Figure 4C), while in gray matter,  $\mu$ FA<sub>DODE</sub> is distributed at much higher values compared to FA<sub>DODE</sub> (Figure 4D). Similar trends were observed for DDE but with  $\mu$ FA or FA shifted towards somewhat higher values (Figures 4E and 4F).

It is also interesting to compare differences between methods within the same tissue type (e.g., comparing same-color distributions down the columns of Figure 4).  $\mu$ FA<sub>DODE</sub> is clearly lower and more widely distributed compared with  $\mu$ FA<sub>DDE</sub> in white matter. In gray matter,  $\mu$ FA<sub>DDE</sub> measured is high, while  $\mu$ FA<sub>DODE</sub> is somewhat smaller. Another interesting finding in gray matter, is that FA<sub>DODE</sub> and FA<sub>DDE</sub> values are only slightly different. The means and standard deviations of  $\mu$ FA and FA for each method are tabulated in Table 1.

A statistical analysis of these data is given in Figure 5, which presents box plots of the data. A one-way ANOVA revealed that in each tissue type (e.g., white matter or gray matter), all four metrics are highly statistically significantly different from each other (corrected  $p < 1e-12$ , post-hoc Bonferroni test). However, it should be noted that although the metrics are different, they are not completely uncorrelated. Table 1 reports Spearman’s  $\rho$  and its significance levels when comparing  $\mu$ FA and FA (extracted by the same method) in each ROI. While  $\mu$ FA<sub>DODE</sub> and FA<sub>DODE</sub> are correlated in white matter (Spearman’s  $\rho = \sim 0.41$ ),  $\mu$ FA<sub>DDE</sub> and FA<sub>DDE</sub> metrics are only weakly correlated (Spearman’s  $\rho = \sim 0.19$ ). In gray matter, the correlations between  $\mu$ FA and FA are weak for both methods and (Spearman’s  $\rho = 0.22$  and  $-0.10$  for DODE and DDE, respectively). Note

that although outlier rejection was used, in all cases less than ~1% of the data were identified as outliers and rejected.

To establish whether and how myelin modulates the anisotropy metrics, Carr-Purcell-Meiboom-Gill (CPMG) MRI experiments were performed on the same slice with the same resolution as the diffusion experiments. To assess the quality of the data, Figures 6A and 6B show the preprocessed data at short and very short TE of 2.9 ms and very long TE of 142.5 ms, respectively, in a representative spinal cord. Even at the very long TE, the SNR remains very high, especially after denoising. Denoising and unringing procedures were validated and found to have no negative impact on the quality of  $T_2$  fitting procedure (data not shown), while improving the fits significantly. Figure 6C shows ROIs drawn in the major tracts of the spinal cord, while Figures 6D and 6E show the  $T_2$  decays (with the ordinate drawn in log scale) and the resultant  $T_2$  spectra (with the abscissa drawn in log scale), respectively. The decays in white matter are clearly non-linear, and the myelin water can be seen as an early peak in the  $T_2$  spectrum with its peak  $T_2$  around ~10 ms.

A representative myelin water fraction (MWF) map arising from pixel-by-pixel quantification of the spectra is shown in Figure 7A. Note the sharp contrast between the different tracts in MWF: for example, the dCST shows the lowest MWF (MWF ~ 0.30) while VST and FC exhibit the highest MWF (MWF ~ 0.45). Scatter plots between MWF and  $\mu$ FA or FA in white matter are shown in Figure 7 for DODE (Figs. 7B) and DDE (Figs. 7C), respectively. Table 2 summarizes the correlation coefficients and associated statistics. A moderate anticorrelation between MWF and  $\mu$ FA<sub>DODE</sub> is observed in the white matter (Spearman's  $\rho = \sim -0.36$ ), while FA<sub>DODE</sub> did not correlate with MWF in a statistically significant manner. The DDE counterparts  $\mu$ FA<sub>DDE</sub> and FA<sub>DDE</sub> exhibited weak anti-correlation and correlation, respectively. Figures 7D and 7E show similar plots as described above, but for gray matter. Notably, correlations between MWF and FA<sub>DODE</sub>, as well as FA<sub>DDE</sub> were very weak and their statistical significance not very high; on the contrary,  $\mu$ FA<sub>DODE</sub> was found to correlate somewhat with MWF, while  $\mu$ FA<sub>DDE</sub> correlated moderately with MWF, with very high statistical significance (c.f. Table 2).

Finally, the correlation of the mean  $\mu$ FA in the different tracts with literature regional averaged axon diameters was assessed. Figures 8A and 8B plot mean  $\mu$ FA and FA against the axon diameters reported in (Dula et al., 2010) for the different spinal cord tracts. These data, along with the values tabulated in Table 3, demonstrate that  $\mu$ FA<sub>DODE</sub> exhibits very strong anticorrelation with axon diameters (Spearman's  $\rho = -0.96$ ,  $p = 0.0028$ ). All other metrics are not significantly correlated with axon diameter.

## Discussion

$\mu$ FA has been recently gaining increasing attention as a potentially useful source of contrast in microstructural MRI due to its ability to disentangle anisotropy from orientation dispersion. Methods other than D(O)DE, such as mapping  $\mu$ FA from experiments tailoring b-tensor shapes are emerging, with many potential applications (De Almeida Martins and Topgaard, 2016; Lasič et al., 2014; Szczepankiewicz et al., 2015; Westin et al., 2016). However, such methods may be confounded by time-dependent diffusion effects (De Swiet and Mitra, 1996; Jespersen et al., 2017c; Vellmer et al., 2017a, 2017b), whereas D(O)DE at long mixing times naturally avoid these confounds (Jespersen, 2012). It is therefore imperative to investigate how  $\mu$ FA may be correlated with underlying microstructural features such as axon dimensions and myelin, much like the early studies aiming to understand the sources for FA (Beaulieu, 2002; Kozlowski et al., 2008a; Mädler et al., 2008; West et al., 2016). In general, perhaps the most significant findings of prior studies on FA (conducted nearly invariably with SDE) were that (1) anisotropy in white matter depends on axonal membranes; and (2) the presence of myelin can further modulate FA metrics (Beaulieu, 2002). The application of oscillating gradients has also been shown to generate more contrast and more accurate estimations of small dimensions as compared to long diffusion time experiments, presumably due to the more efficient probing of smaller dimensions via the shorter diffusion times (Álvarez et al., 2013; Jiang et al., 2016; Xu et al., 2014).

The present study aimed to investigate how  $\mu$ FA differs from FA in terms of correlations with myelin water and axonal diameters, and to compare those metrics when measured with DDE or DODE sequences. We first focus attention to our results arising from white matter tissue. Notably,  $\mu$ FA was always larger than FA (Figures 3-5 and Table 2), in agreement with previous DDE experiments in fixed tissues (Jespersen et al., 2013) and in-vivo (Lawrenz et al., 2016). Since the  $\mu$ FA and FA metrics were extracted from the same acquisition, it is unlikely that other effects such as exchange or relaxation contributed to  $\mu$ FA > FA. Thus, our finding supports the notion that that orientation dispersion is significant even in highly structured tissues, such as spinal cord white matter. This is in excellent agreement with a recent study of SDE-derived diffusion tensor and kurtosis time-dependencies which also pointed to the same conclusion in pig spinal cord (Jespersen et al., 2017a), as well as with histological studies attempting to measure the dispersion directly in white matter (Leergaard et al., 2010). It is difficult to draw conclusions on whether the orientation dispersion arises within intra- or extra-axonal spaces (or both), or, whether undulations (Nilsson et al., 2012) or passing collateral fibers (Lundell et al., 2011) can contribute to these observations. Performing similar spectroscopic measurements utilizing cell-specific markers such as NAA or mI (Shemesh et al., 2014b, 2017), or performing much more extensive time/frequency/b-value-dependent measurements on water (Veraart et al., 2016a) (Papaioannou et al., 2017; Reynaud et al., 2016), or on metabolites (Palombo et al., 2016a; Valette et al., 2018) may further assist in addressing this question in the future.

Another interesting aspect when comparing  $\mu$ FA with FA in white matter, is that the two metrics are only moderately correlated when measured with DODE, and very weakly correlated when measured with DDE (c.f. Table 1). This finding suggests that when diffusion is encoded using oscillating gradients, spins experience less orientation dispersion than when they are probed using block gradients, since  $\mu$ FA would be perfectly correlated (and identical) to FA for perfectly aligned fibers. Hence, our findings point to specific length scales for orientation dispersion that are probed differently using the different sequences.

Next, we consider the relationships between myelin and  $\mu\text{FA}$ . Akin to its FA counterpart –  $\mu\text{FA}$  is ambiguous in that a compartment with length ‘L’ and radius ‘R’ can give rise to the same  $\mu\text{FA}$  as a compartment with length 2L and radius 2R. The axial path length could be restricted due to nodes of Ranvier, non-ideal cylindrical structure, varicosities, etc. However, if the path length parallel to the (assumably) ellipsoids is constant, then one could predict that when larger amounts of myelin surround an axon, the  $\mu\text{FA}$  will be smaller as the restriction will increase in the perpendicular direction. However, in our study, a moderate *negative* correlation was observed between MWF and  $\mu\text{FA}_{\text{DODE}}$  in white matter (Figure 7 and Table 2). This can be fully explained by considering the dependence of MWF and axon diameter via the g-ratio (Guy et al., 1989): the larger the axon, the thicker the myelin around it in (healthy) mammalian white matter (Innocenti, 2011). Hence, the negative correlation between  $\mu\text{FA}_{\text{DODE}}$  and MWF would reflect indirectly the approximately constant g-ratio in healthy tissue, rather than enhanced restriction. Interestingly,  $\mu\text{FA}_{\text{DDE}}$  showed a much weaker, yet still negative correlation with MWF. Since the microstructure has not changed between measurements, this likely reflects that DODE and DDE probe different path lengths *parallel* to the spinal cord’s major axis: the larger the diffusion time, the longer path will be probed in the unrestricted dimension, and thence the  $\mu\text{FA}$  will be larger and less reflective of axon diameter or, by proxy, its myelin thickness.  $\text{FA}_{\text{DDE}}$  showed a small positive correlation with MWF, which perhaps reflects the ambiguity of probing restriction and orientation distribution at the same time. Extracellular space contributions again cannot be neglected here, but for coherently aligned systems the arguments are similar as one could potentially treat the space between densely packed axons as potentially even more restricted than the intra-axonal space itself (Shemesh et al., 2011). It is also worth mentioning that MWF extracted from multiexponential  $T_2$  measurements, as performed in this study, have been shown in the past to reflect microstructural metrics such as axon size and myelin thickness very faithfully in white matter (Dula et al., 2010; Kozlowski et al., 2008a; MacKay et al., 2006).

Our most striking findings in this study, perhaps, is that  $\mu\text{FA}_{\text{DODE}}$  showed an extremely high, and statistically significant, negative correlation with axon diameters reported by (Harkins et al., 2016) for the different tracts (Table 3). This observation lends further credence to the explanation above: the finite parallel length scale probed by DODE makes the measurement strongly dependent on the perpendicular restriction, which in this case is reflected through axon sizes. Although the axon diameters were obtained from literature, it is worth stressing that axon diameter dependence in healthy spinal cords is highly reproducible and that the tracts analyzed were obtained from very similar cervical slices as in (Dula et al., 2010). Such a strong correlation is also highly unlikely to be obtained randomly. It is very interesting to also note that all other metrics did not correlate in a statistically significant fashion with axon diameters:  $\mu\text{FA}_{\text{DDE}}$  likely due to its probing of longer parallel lengths, and the FA from both methods due to its inherent conflation or restriction with orientation dispersion.

In the spinal cord gray matter, very low  $\text{FA}_{\text{DODE}}$  and  $\text{FA}_{\text{DDE}}$  values were measured, suggesting a much lower degree of restriction compared to white matter diffusion. However, the  $\mu\text{FA}_{\text{DODE}}$  and  $\mu\text{FA}_{\text{DDE}}$  metrics in gray matter were still very high in the gray matter. In fact, the values reported in Table 1 also reflect  $\frac{\mu\text{FA}_{\text{DODE}}^{\text{GM}}}{\mu\text{FA}_{\text{DODE}}^{\text{WM}}} = \sim 0.92$  and  $\frac{\mu\text{FA}_{\text{DDE}}^{\text{GM}}}{\mu\text{FA}_{\text{DDE}}^{\text{WM}}} = \sim 0.89$ . Combined with the low FA values in the gray matter, our findings suggest that a significant component of gray matter tissue experiences restricted diffusion but with a large degree of orientation dispersion. This finding is also in good agreement with previous literature demonstrating significant angular DDE

modulations in ex-vivo gray matter (Shemesh et al., 2011; Shemesh and Cohen, 2011a). Further studies are needed to establish which underlying biological components give rise to such high  $\mu\text{FA}$  in gray matter, but dendrites, astrocyte branches, and nonmyelinated or myelinated axons traversing gray matter could be suspected (Palombo et al., 2016b, 2017). Time-dependent or spectroscopic experiments on metabolites could provide insight into such questions in the future.

Several limitations can be identified in this study. First, we have introduced a new way of measuring  $\mu\widetilde{A}^2$  harnessing the 5-design acquisition at two b-values to reduce the recently-reported bias in  $\mu A^2$  estimation due to higher order terms. Our new method is likely inferior to a sampling of a large range of b-values and the ensuing polynomial fitting as done in Ianuş et al (Ianuş et al., 2017a). However, the advantage of the current approach is that it manages to avoid a prohibitively long experiment duration. Future studies will identify the accuracy and precision of the method proposed above vis-à-vis the ground-truth, and attempt to find optimal b-values for measuring  $\mu\widetilde{A}^2$  as accurately and with as little bias as possible. Second, to compute  $\mu\text{FA}$ , we executed a third measurement at lower b-value to extract  $MD$ , which is then input into Eq. 2 along with  $\mu\widetilde{A}^2$ . However,  $MD$  itself may be conflated with higher-order terms, as pointed out recently by (Chuhutin et al., 2017); in this study, this issue was not accounted for, and may induce minor biases in the measurements of  $\mu\text{FA}$ . Better estimation of  $MD$  could probably be performed by sampling one or more low b-values and fitting kurtosis and  $MD$  at the same time from spherically averaged data. In addition, we have not explored the impact of specific b-value selection. At too low b-values, the difference in the log signals is very small, while at higher b-values, even higher-order terms may come into play. Third, the sample size was quite small ( $N = 2$  spinal cords, only a single slice per cord), such that the variability across animals was not very well sampled. However, it is worth noting that the results were actually very consistent between both spinal cords: the mean  $\mu\text{FA}$  and  $\text{FA}$ , for both DODE and DDE, varied less than 10% between the cords (both in gray and white matter tissues), and the MWF varied less than 6% between the tissues. Although this consistency is promising for the robustness of the approach, the small number of samples renders this study perhaps more exploratory. Fourth, the experiments were performed at a relatively long TE of 52 ms. Given that the MWF was associated with  $T_2 < 20$  ms and that the other water  $T_2$ s were distributed between  $\sim 20$ -60 ms, the experiments can be considered completely filtered for (directly

contributing) myelin water, as  $e^{\frac{-TE}{T_{2\text{myelin}}}} \sim 0.005$ . Exchange between myelin water and intra/extra-axonal water is highly likely to occur, which may also confound the measurements, although it should be noted that at least for conventional DODE MRI, the relatively long TE is nearly unavoidable due to the necessity of non-negligible diffusion gradient waveform durations. Double-stimulated-echo approaches (Jerschow, A, Muller, 1997; Shemesh and Cohen, 2011b) would thus be nearly impossible to execute for DODE, even before considering the significant SNR reduction associated with such sequences,  $(1/2)^N$ , where  $N$  is the number of stimulated echoes. Finally, a histological study was not here performed, and the study relies on literature reports of correlations between MRI-derived MWF and myelin thickness and the values for axon diameters. Future studies can expand the findings here and perform more direct correlations with histology, although it should be pointed out that big differences in these parameters are unlikely to be observed for healthy tissues. In addition, it would be fruitful to modulate the microstructure actively and to observe how  $\mu\text{FA}$  varies, e.g., using genetic mutations that alter myelin content. All these highly interesting avenues will be pursued in the future, but the present study provides the first steps in this direction.

## Conclusions

This study investigated the microstructural correlates of  $\mu$ FA and FA using high resolution D(O)DE experiments in fixed spinal cords at 16.4 T. Our results indicate very strong anticorrelations of  $\mu$ FA<sub>DODE</sub> with axon size, and moderate anticorrelations of  $\mu$ FA<sub>DODE</sub> with MWF, whereas  $\mu$ FA<sub>DDE</sub>, FA<sub>DODE</sub> and FA<sub>DDE</sub> correlate to a much lesser or no extent with those microstructural features. These findings shed light on the mechanisms of restriction in spinal cord white matter when investigate without conflation by orientation dispersion. The correlations of  $\mu$ FA<sub>DODE</sub> with axon diameters and myelin water fraction are thus promising for future investigations of longitudinal variations in these properties, e.g., in disease or with learning.



## **Acknowledgements**

This study was funded in part by the European Research Council (ERC) under the European Union's Horizon 2020 research and innovation programme (grant agreement No. 679058 - DIRECT-fMRI). The author would like to thank Prof. Sune N Jespersen and Mr. Jonas Lynge Olesen (Aarhus University) for providing the codes for denoising and Gibbs unringing, as well as for many insightful discussions. The author also thanks Dr. Daniel Nunes for extracting the tissues used in this study, Dr. Andrada Ianus and Ms. Teresa Serradas Duarte for providing parts of code used in the analyses performed here, and Prof. Mark D Does from Vanderbilt University for the REMMI pulse sequence and its analysis tools, that were supported through grant number NIH EB019980.

## **Author contribution statement**

NS designed the study, collected and analyzed data, and wrote the paper.

## **Conflicts of Interest**

The author declares no conflict of interest.

## Figures

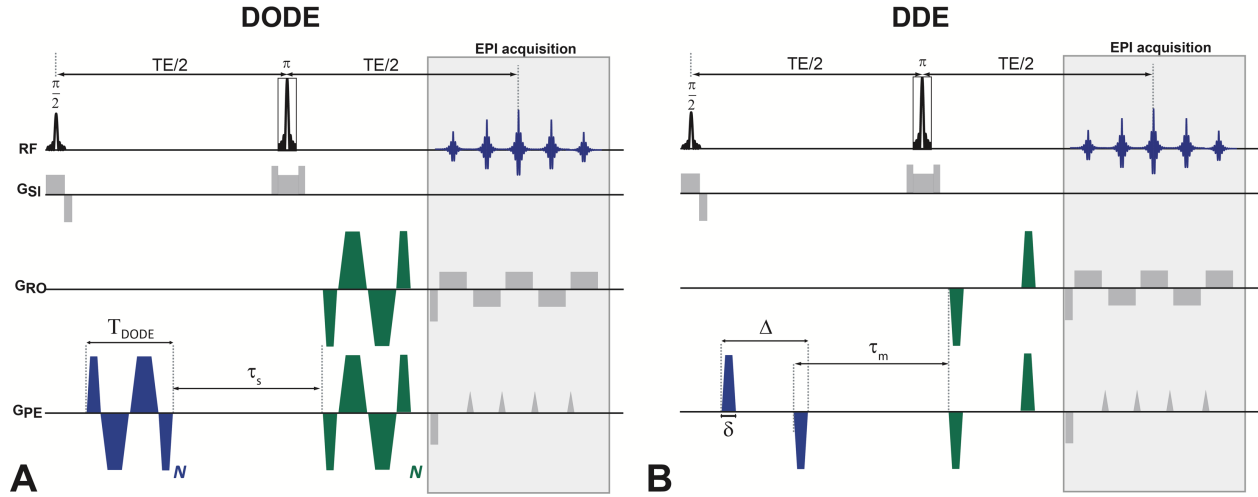


**Figure 1.** Diffusion MRI pulse sequences used in this study. **(A)** DODE and **(B)** DDE weightings were overlaid on a basic SE-EPI sequence. The diffusion gradient orientations are independent and can vary in any of the axes, the particular instantiation here represents one particular case where  $\mathbf{G}_1$  is oriented along the PE axis and  $\mathbf{G}_2$  is at an angle in the PE-RO plane. Other than the relative orientations that varied, identical waveforms were used for the two diffusion encodings.

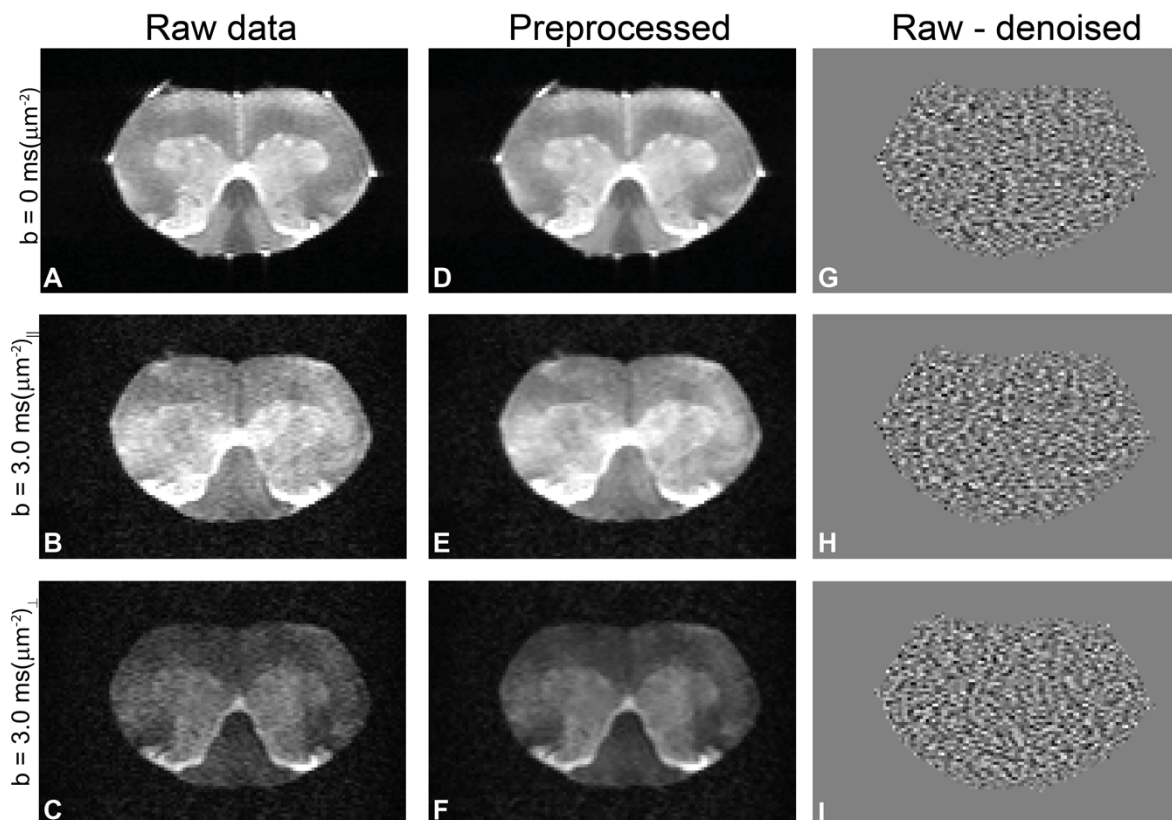


**Figure 2.** Quality of diffusion MRI data and preprocessing in a representative spinal cord. **(A-C)** Raw data with zero b-value, parallel, and perpendicular waveforms acquired at the highest b-value, respectively. The perpendicular waveform had more significant components along the spinal cord principal axis and thus show greater attenuation. **(D-F)** Results of preprocessing the data in A-C (denoising and Gibbs unringing). Notice how the noise is highly reduced in the preprocessed images without adverse effects to image quality. **(G-I)** Subtraction of denoised and raw data, showing only noise and thus demonstrating that no significant signal components were removed during Marchenko-Pastur PCA denoising.

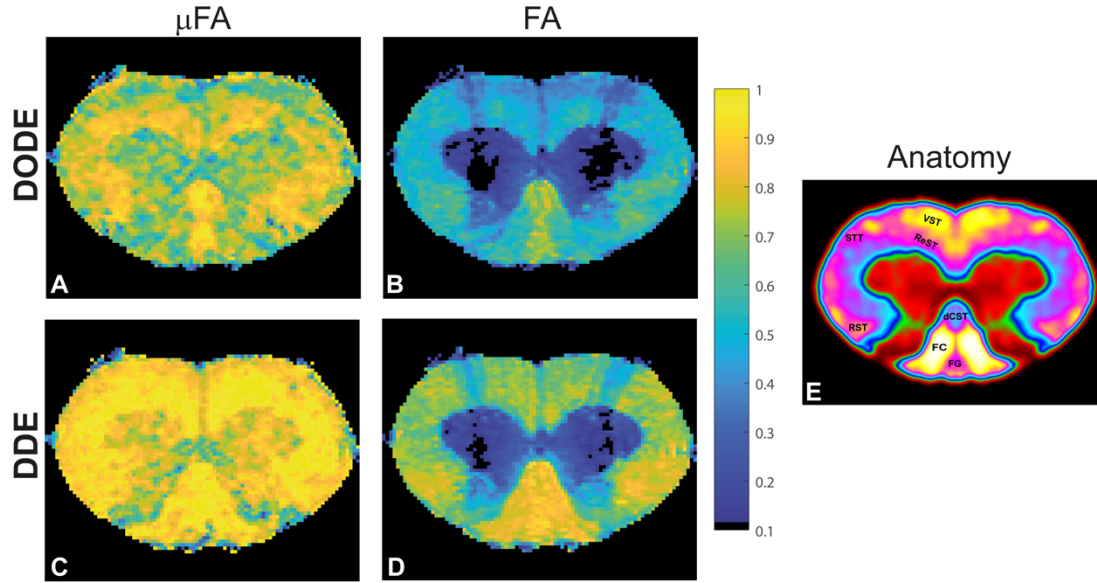


**Figure 3.** Parameter maps for a representative spinal cord. (A)  $\mu\text{FA}_{\text{DODE}}$ ; (B)  $\text{FA}_{\text{DODE}}$ ; (C)  $\mu\text{FA}_{\text{DDE}}$ ; (D)  $\text{FA}_{\text{DDE}}$ . Notice the differences in contrast both in white and in gray matter tissues both between metrics and between sequences. Most notably,  $\mu\text{FA}$  is higher than FA and DDE-driven metrics are higher than DODE-driven metrics, especially in white matter. (E) Anatomy of the spinal cord for reference, displayed over a smoothed false-color image of the cervical segment. The gray matter is shown in red and green, while the tracts are highlighted on the left side of the cord.

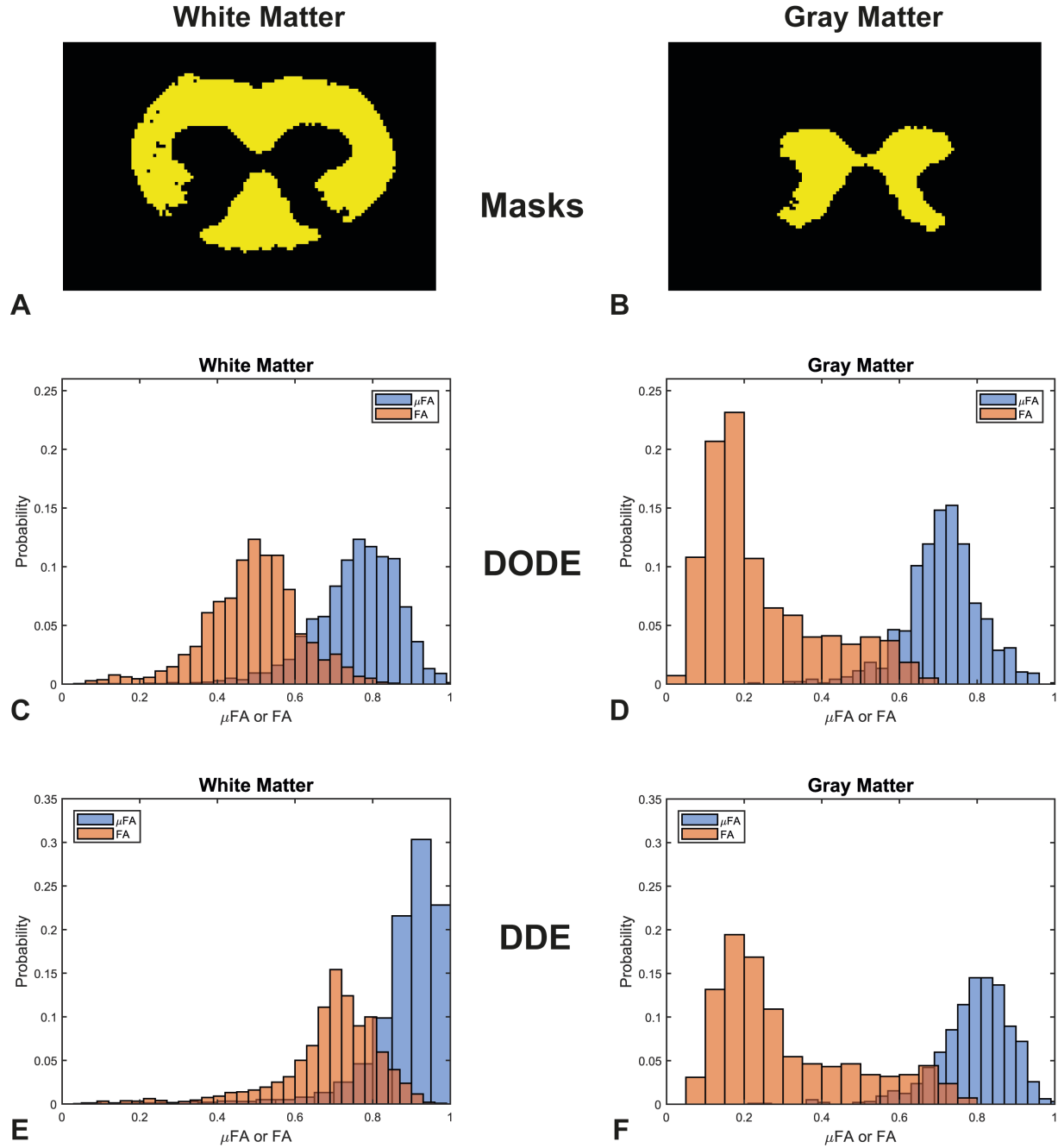


**Figure 4.** Histogram distributions of the different metrics in white matter and gray matter. **(A-B)** Masks for the white and gray matter tissues, respectively. **(C-D)**  $\mu\text{FA}_{\text{DODE}}$  and  $\text{FA}_{\text{DODE}}$  for white and gray matter. **(E-F)**  $\mu\text{FA}_{\text{DDE}}$  and  $\text{FA}_{\text{DDE}}$  for white and gray matter. Notice the different distributions in white matter for both DODE- and DDE-driven metrics, as well as the higher  $\mu\text{FA}$  as compared to  $\text{FA}$  in all tissues.

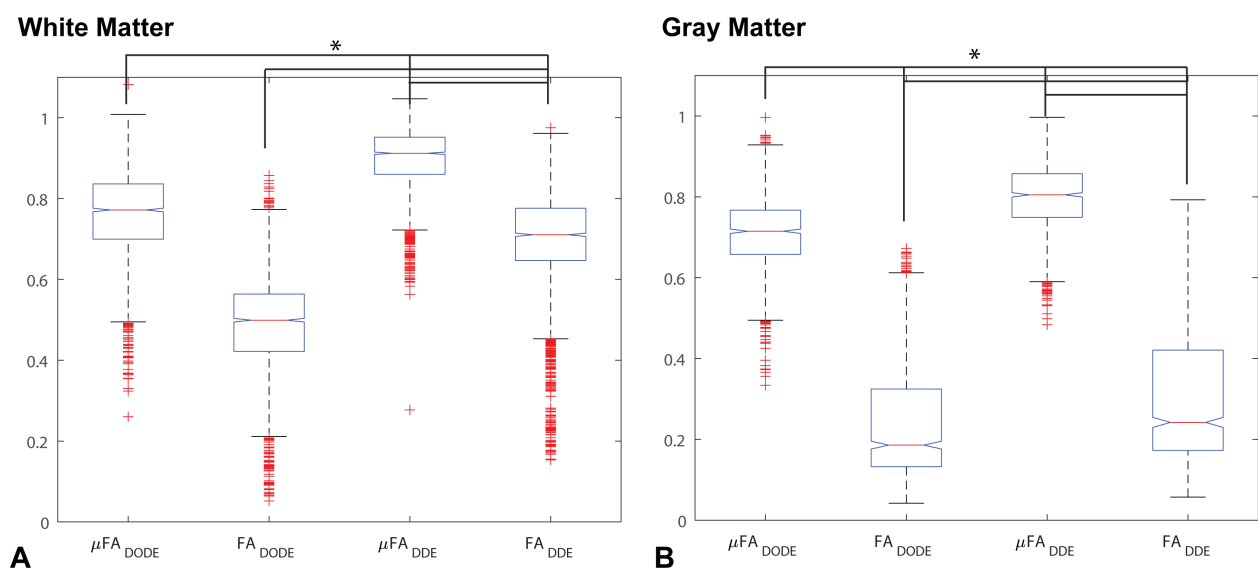


**Figure 5.** Box-and-whisker plots of the different metrics. **(A)** White matter analysis. **(B)** Gray matter analysis.  $*p < 10^{-12}$  between all pairs from ANOVA with Bonferroni post-hoc comparison and corrected for multiple comparisons.

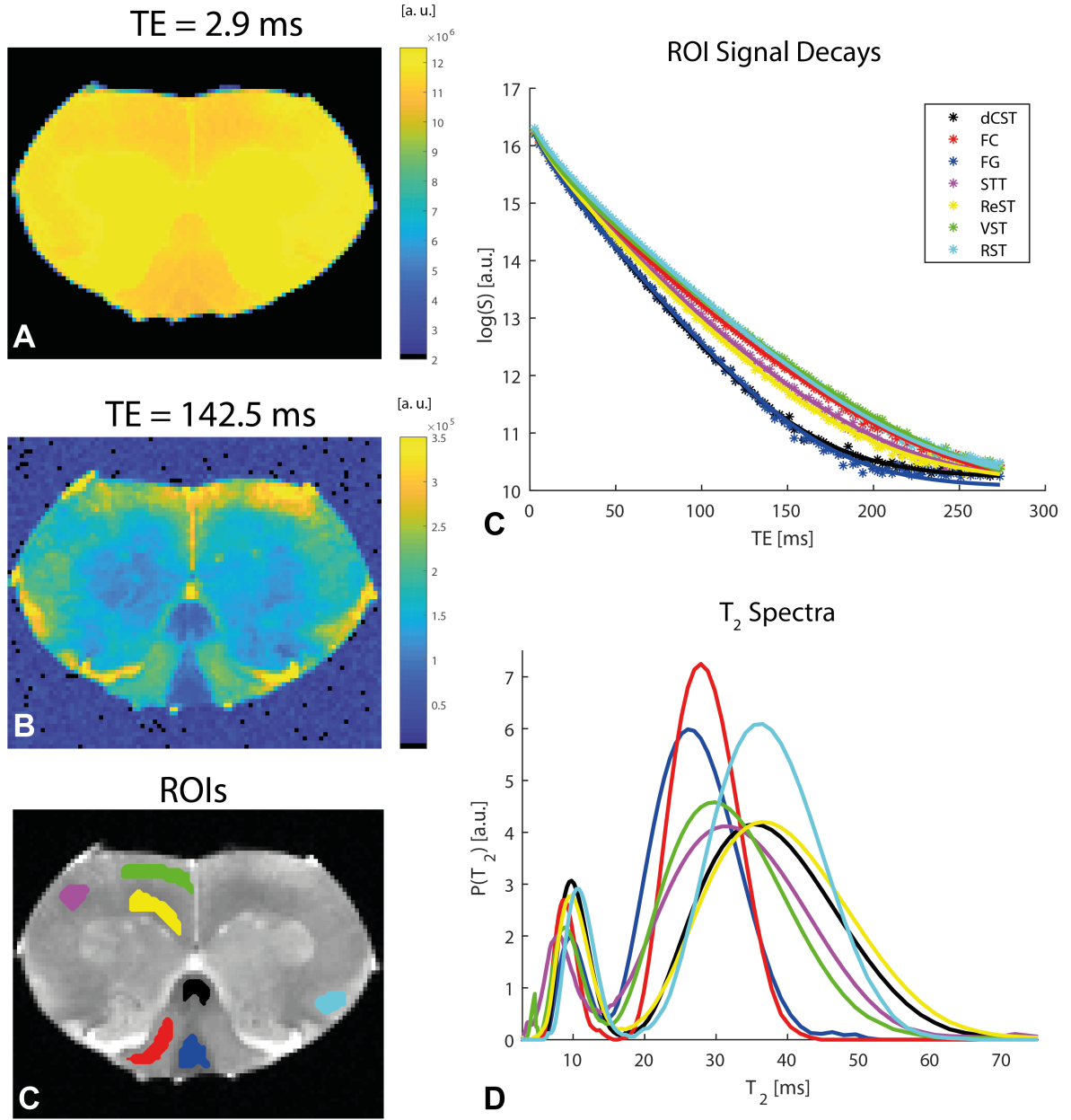


**Figure 6.** Relaxation data and analysis in a representative spinal cord. **(A-B)** Preprocessed data at short and long TEs, respectively, reveal excellent SNR. **(C)** ROI definitions. **(D)** Mean ROI signal decays with TE (symbols) along with their respective fits (solid lines). N.b. the log scale in the ordinate. **(E)**  $T_2$  spectra (plotted in log scale in the abscissa) extracted from an iLT fit to the ROI data. The myelin water is associated with the peak corresponding to shorter  $T_2$  values. The ROI colors in (C) correspond to the color of the plots in (D-E).

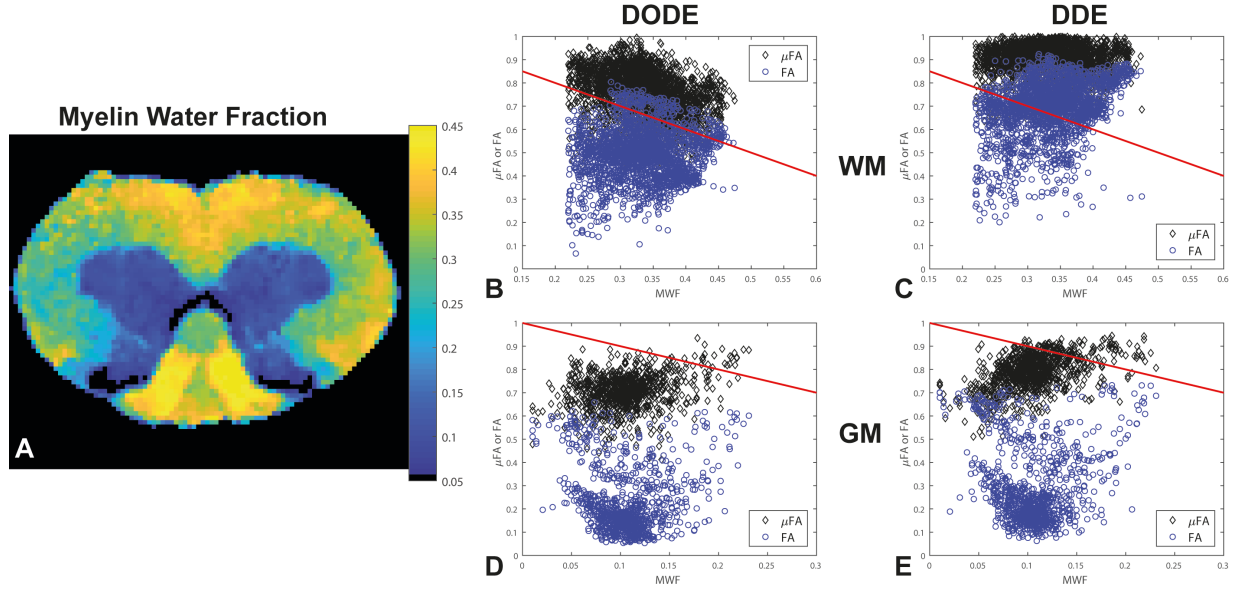


**Figure 7.** Myelin Water Fraction (MWF) and its correlations with diffusion-derived metrics. **(A)** MWF from a representative spinal cord, showing excellent contrast between the white matter and gray matter as well as within most white matter tracts. **(B-E)** Correlations between DODE and DDE metrics with MWF in white and gray matter tissues. Blue circles represent FA whereas black diamonds represent  $\mu$ FA. Red lines represent  $-1 \times \text{identity}$  to guide the eye.

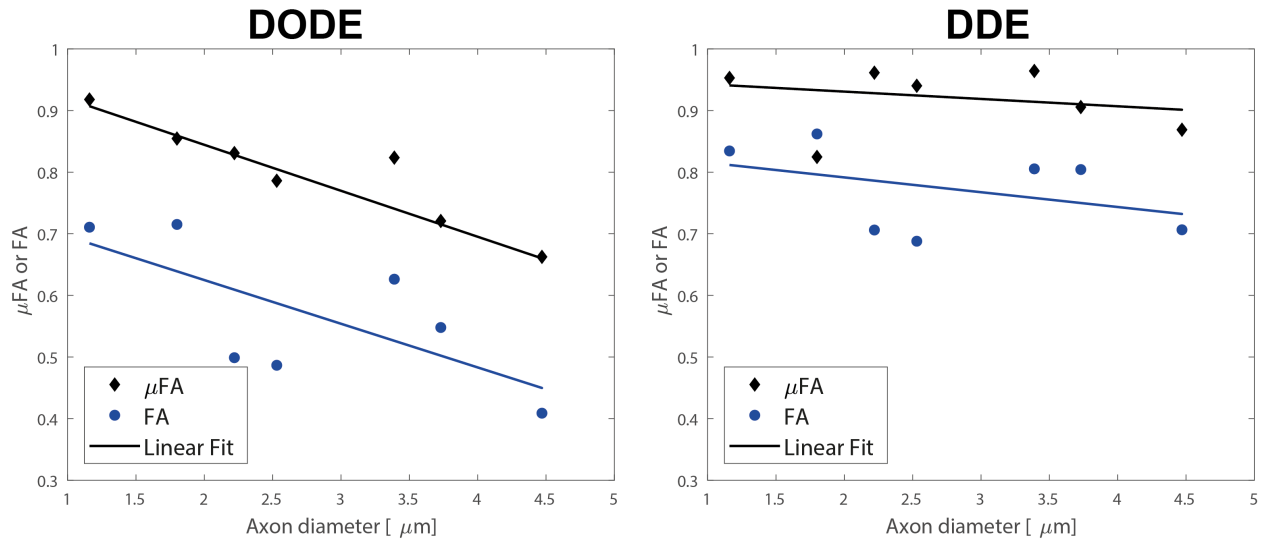


**Figure 8.** Correlations of diffusion metrics with literature-based average axon diameters in the different white matter tracts. **(A)** Correlations of metrics derived from DODE. **(B)** Correlations derived from DDE. The best linear regressions to the experimental data are also given as solid lines. Note the excellent inverse agreement between  $\mu\text{FA}_{\text{DODE}}$  and axon diameter, which also had a very high anticorrelation coefficient of  $\rho \sim -0.96$  while all other metrics did not show significant correlations.



## References

- Álvarez, G. A., Shemesh, N., and Frydman, L. (2013). Coherent dynamical recoupling of diffusion-driven decoherence in magnetic resonance. *Phys. Rev. Lett.* 111.
- Assaf, Y., Alexander, D. C., Jones, D. K., Bizzi, A., Behrens, T. E. J., Clark, C. A., et al. (2013). The CONNECT project: Combining macro- and micro-structure. *Neuroimage* 80. doi:10.1016/j.neuroimage.2013.05.055.
- Avram, A. V., Özarslan, E., Sarlls, J. E., and Basser, P. J. (2013). In vivo detection of microscopic anisotropy using quadruple pulsed-field gradient (qPFG) diffusion MRI on a clinical scanner. *Neuroimage* 64, 229–239. doi:10.1016/j.neuroimage.2012.08.048.
- Basser, P. J., and Jones, D. K. (2002). Diffusion-tensor MRI: Theory, experimental design and data analysis - A technical review. *NMR Biomed.* 15, 456–467. doi:10.1002/nbm.783.
- Beaulieu, C. (2002). The basis of anisotropic water diffusion in the nervous system - A technical review. *NMR Biomed.* 15, 435–455. doi:10.1002/nbm.782.
- Callaghan, P. T., Coy, A., MacGowan, D., Packer, K. J., and Zelaya, F. O. (1991). Diffraction-like effects in NMR diffusion studies of fluids in porous solids. *Nature* 351, 467–469. doi:10.1038/351467a0.
- Callaghan, P. T., and Komlosh, M. E. (2002). Locally anisotropic motion in a macroscopically isotropic system: Displacement correlations measured using double pulsed gradient spin-echo NMR. *Magn. Reson. Chem.* 40, 15–19. doi:10.1002/mrc.1122.
- Cheng, Y., and Cory, D. G. (1999). Multiple scattering by NMR. *J. Am. Chem. Soc.* 121, 7935–7936. doi:10.1021/ja9843324.
- Chuhutin, A., Hansen, B., and Jespersen, S. N. (2017). Precision and accuracy of diffusion kurtosis estimation and the influence of b-value selection. *NMR Biomed.* 30, 1–14. doi:10.1002/nbm.3777.
- Clark, C. A., Hedehus, M., and Moseley, M. E. (2001). Diffusion time dependence of the apparent diffusion tensor in healthy human brain and white matter disease. *Magn. Reson. Med.* 45, 1126–1129. doi:10.1002/mrm.1149.
- Cohen, Y., and Assaf, Y. (2002). High b-value q-space analyzed diffusion-weighted MRS and MRI in neuronal tissues - A technical review. *NMR Biomed.* 15, 516–542. doi:10.1002/nbm.778.
- Cory, DG, Garroway, AN, Miller, J. (1990). Applications of Spin Transport as a probe of local geometry.
- De Almeida Martins, J. P., and Topgaard, D. (2016). Two-Dimensional Correlation of Isotropic and Directional Diffusion Using NMR. *Phys. Rev. Lett.* 116, 1–6. doi:10.1103/PhysRevLett.116.087601.
- De Swiet, T. M., and Mitra, P. P. (1996). Possible systematic errors in single-shot measurements of the trace of the diffusion tensor. *J. Magn. Reson. - Ser. B* 111, 15–22. doi:10.1006/jmrb.1996.0055.
- Does, M. D., Parsons, E. C., and Gore, J. C. (2003). Oscillating gradient measurements of water diffusion in normal and globally ischemic rat brain. *Magn. Reson. Med.* 49, 206–215. doi:10.1002/mrm.10385.
- Drobnjak, I., Zhang, H., Ianuş, A., Kaden, E., and Alexander, D. C. (2016). PGSE, OGSE, and sensitivity to axon diameter in diffusion MRI: Insight from a simulation study. *Magn. Reson. Med.* 75, 688–700. doi:10.1002/mrm.25631.
- Dula, A. N., Gochberg, D. F., Valentine, H. L., Valentine, W. M., and Does, M. D. (2010).

- Multiexponential T2, magnetization transfer, and Quantitative histology in white matter tracts of rat spinal cord. *Magn. Reson. Med.* 63, 902–909. doi:10.1002/mrm.22267.
- Eichner, C., Cauley, S. F., Cohen-Adad, J., Möller, H. E., Turner, R., Setsompop, K., et al. (2015). Real diffusion-weighted MRI enabling true signal averaging and increased diffusion contrast. *Neuroimage* 122, 373–384. doi:10.1016/j.neuroimage.2015.07.074.
- Fieremans, E., Burcaw, L. M., Lee, H. H., Lemberskiy, G., Veraart, J., and Novikov, D. S. (2016). In vivo observation and biophysical interpretation of time-dependent diffusion in human white matter. *Neuroimage* 129, 414–427. doi:10.1016/j.neuroimage.2016.01.018.
- Finsterbusch, J. (2011). *Multiple-Wave-Vector Diffusion-Weighted NMR*. 1st ed. Elsevier Ltd. doi:10.1016/B978-0-12-385857-3.00006-2.
- Gore, J. C., Xu, J., Colvin, D. C., Yankeelov, T. E., Parsons, E. C., and Does, M. D. (2010). Characterization of tissue structure at varying length scales using temporal diffusion spectroscopy. *NMR Biomed.* 23, 745–756. doi:10.1002/nbm.1531.
- Grebenkov, D. S. (2007). NMR survey of reflected Brownian motion. *Rev. Mod. Phys.* 79, 1077–1137. doi:10.1103/RevModPhys.79.1077.
- Guizar-Sicairos, M., Thurman, S. T., and Fienup, J. R. (2008). Efficient subpixel image registration algorithms. *Opt. Lett.* 33, 156. doi:10.1364/OL.33.000156.
- Guy, J., Ellis, E. A., Kelley, K., and Hope, G. M. (1989). Spectra of G ratio, myelin sheath thickness, and axon and fiber diameter in the guinea pig optic nerve. *J. Comp. Neurol.* 287, 446–454. doi:10.1002/cne.902870404.
- Harkins, K. D., Xu, J., Dula, A. N., Li, K., Valentine, W. M., Gochberg, D. F., et al. (2016). The microstructural correlates of T1 in white matter. *Magn. Reson. Med.* 75, 1341–1345. doi:10.1002/mrm.25709.
- Ianuș, A., Jespersen, S. N., Serradas, T., and Alexander, D. C. (2017a). Accurate estimation of microscopic diffusion anisotropy and its time dependence in the mouse brain. *Arxiv*.
- Ianuș, A., Shemesh, N., Alexander, D. C., and Drobnjak, I. (2017b). Double oscillating diffusion encoding and sensitivity to microscopic anisotropy. *Magn. Reson. Med.* 78, 550–564. doi:10.1002/mrm.26393.
- Innocenti, G. M. (2011). Development and evolution. Two determinants of cortical connectivity. *Prog. Brain Res.* 189, 65–75. doi:10.1016/B978-0-444-53884-0.00018-X.
- Jerschow, A., Muller, N. (1997). Suppression of Convection Artifacts in Stimulated-Echo Diffusion Experiments. Double-Stimulated-Echo Experiments ALEXEJ. 375, 372–375.
- Jespersen, S. N. (2012). Equivalence of double and single wave vector diffusion contrast at low diffusion weighting. *NMR Biomed.* 25, 813–818. doi:10.1002/nbm.1808.
- Jespersen, S. N., Bjarkam, C. R., Nyengaard, J. R., Chakravarty, M. M., Hansen, B., Vosegaard, T., et al. (2010). Neurite density from magnetic resonance diffusion measurements at ultrahigh field: Comparison with light microscopy and electron microscopy. *Neuroimage* 49, 205–216. doi:10.1016/j.neuroimage.2009.08.053.
- Jespersen, S. N., Kroenke, C. D., Østergaard, L., Ackerman, J. J. H., and Yablonskiy, D. A. (2007). Modeling dendrite density from magnetic resonance diffusion measurements. *Neuroimage* 34, 1473–1486. doi:10.1016/j.neuroimage.2006.10.037.
- Jespersen, S. N., Lundell, H., Sønderby, C. K., and Dyrby, T. B. (2013). Orientationally invariant metrics of apparent compartment eccentricity from double pulsed field gradient diffusion experiments. *NMR Biomed.* 26, 1647–1662. doi:10.1002/nbm.2999.
- Jespersen, S. N., Olesen, J. L., Hansen, B., and Shemesh, N. (2017a). Diffusion time dependence of microstructural parameters in fixed spinal cord. *Neuroimage*.

- doi:10.1016/j.neuroimage.2017.08.039.
- Jespersen, S. N., Olesen, J. L., Hansen, B., and Shemesh, N. (2017b). Diffusion time dependence of microstructural parameters in fixed spinal cord. *Neuroimage*, 1–14. doi:10.1016/j.neuroimage.2017.08.039.
- Jespersen, S. N., Olesen, J. L., Ianu, A., and Shemesh, N. (2017c). Anisotropy in “ isotropic diffusion “ measurements due to nongaussian diffusion. *arXiv*, 1–22.
- Jiang, X., Li, H., Xie, J., Zhao, P., Gore, J. C., and Xu, J. (2016). Quantification of cell size using temporal diffusion spectroscopy. *Magn. Reson. Med.* 75, 1076–1085. doi:10.1002/mrm.25684.
- Johansen-Berg, H., Behrens, T. (2009). *Diffusion MRI: From quantitative measurement to in vivo neuroanatomy*.
- Kellner, E., Dhital, B., Kiselev, V. G., and Reisert, M. (2016). Gibbs-ringing artifact removal based on local subvoxel-shifts. *Magn. Reson. Med.* 76, 1574–1581. doi:10.1002/mrm.26054.
- Klawiter, E. C., Schmidt, R. E., Trinkaus, K., Liang, H. F., Budde, M. D., Naismith, R. T., et al. (2011). Radial diffusivity predicts demyelination in ex vivo multiple sclerosis spinal cords. *Neuroimage* 55, 1454–1460. doi:10.1016/j.neuroimage.2011.01.007.
- Koch, M. A., and Finsterbusch, J. (2008). Compartment size estimation with double wave vector diffusion-weighted imaging. *Magn. Reson. Med.* 60, 90–101. doi:10.1002/mrm.21514.
- Koch, M. A., and Finsterbusch, J. (2011). Towards compartment size estimation in vivo based on double wave vector diffusion weighting. *NMR Biomed.* 24, 1422–1432. doi:10.1002/nbm.1711.
- Komlosh, M. E., Lizak, M. J., Horkay, F., Freidlin, R. Z., and Basser, P. J. (2008). Observation of microscopic diffusion anisotropy in the spinal cord using double-pulsed gradient spin echo MRI. *Magn. Reson. Med.* 59, 803–809. doi:10.1002/mrm.21528.
- Komlosh, M. E., Özarslan, E., Lizak, M. J., Horkay, F., Schram, V., Shemesh, N., et al. (2011). Pore diameter mapping using double pulsed-field gradient MRI and its validation using a novel glass capillary array phantom. *J. Magn. Reson.* 208. doi:10.1016/j.jmr.2010.10.014.
- Kozlowski, P., Liu, J., Yung, A. C., and Tetzlaff, W. (2008a). High-resolution myelin water measurements in rat spinal cord. *Magn. Reson. Med.* 59, 796–802. doi:10.1002/mrm.21527.
- Kozlowski, P., Raj, D., Liu, J., Lam, C., Yung, A. C., and Tetzlaff, W. (2008b). Characterizing White Matter Damage in Rat Spinal Cord with Quantitative MRI and Histology. *J. Neurotrauma* 25, 653–676. doi:10.1089/neu.2007.0462.
- Lasič, S., Szczepankiewicz, F., Eriksson, S., Nilsson, M., and Topgaard, D. (2014). Microanisotropy imaging: quantification of microscopic diffusion anisotropy and orientational order parameter by diffusion MRI with magic-angle spinning of the q-vector. *Front. Phys.* 2, 1–14. doi:10.3389/fphy.2014.00011.
- Latour, L. L., Svoboda, K., Mitra, P. P., and Sotak, C. H. (1994). Time-dependent diffusion of water in a biological model system. *Proc. Natl. Acad. Sci.* 91, 1229–1233. doi:10.1073/pnas.91.4.1229.
- Laun, F. B., Kuder, T. A., Semmler, W., and Stieltjes, B. (2011). Determination of the defining boundary in nuclear magnetic resonance diffusion experiments. *Phys. Rev. Lett.* 107, 2–5. doi:10.1103/PhysRevLett.107.048102.
- Laun, F. B., Kuder, T. A., Wetscherek, A., Stieltjes, B., and Semmler, W. (2012). NMR-based diffusion pore imaging. *Phys. Rev. E - Stat. Nonlinear, Soft Matter Phys.* 86, 1–23. doi:10.1103/PhysRevE.86.021906.

- Lawrenz, M., Brassen, S., and Finsterbusch, J. (2016). Microscopic diffusion anisotropy in the human brain: Age-related changes. *Neuroimage* 141, 313–325. doi:10.1016/j.neuroimage.2016.07.031.
- Lawrenz, M., and Finsterbusch, J. (2015). Mapping measures of microscopic diffusion anisotropy in human brain white matter in vivo with double-wave-vector diffusion-weighted imaging. *Magn. Reson. Med.* 73, 773–783. doi:10.1002/mrm.25140.
- Lawrenz, M., Koch, M. A., and Finsterbusch, J. (2010). A tensor model and measures of microscopic anisotropy for double-wave-vector diffusion-weighting experiments with long mixing times. *J. Magn. Reson.* 202, 43–56. doi:10.1016/j.jmr.2009.09.015.
- Leergaard, T. B., White, N. S., De Crespigny, A., Bolstad, I., D'Arceuil, H., Bjaalie, J. G., et al. (2010). Quantitative histological validation of diffusion MRI fiber orientation distributions in the rat brain. *PLoS One* 5, 1–8. doi:10.1371/journal.pone.0008595.
- Lundell, H., Nielsen, J. B., Ptito, M., and Dyrby, T. B. (2011). Distribution of collateral fibers in the monkey cervical spinal cord detected with diffusion-weighted magnetic resonance imaging. *Neuroimage* 56, 923–929. doi:10.1016/j.neuroimage.2011.02.043.
- Mädler, B., Drabycz, S. A., Kolind, S. H., Whittall, K. P., and MacKay, A. L. (2008). Is diffusion anisotropy an accurate monitor of myelination?. Correlation of multicomponent T2 relaxation and diffusion tensor anisotropy in human brain. *Magn. Reson. Imaging* 26, 874–888. doi:10.1016/j.mri.2008.01.047.
- MacKay, A., Laule, C., Vavasour, I., Bjarnason, T., Kolind, S., and Mädler, B. (2006). Insights into brain microstructure from the T2 distribution. *Magn. Reson. Imaging* 24, 515–525. doi:10.1016/j.mri.2005.12.037.
- Mitra, P. P. (1995). Multiple wave-vector extensions of the NMR pulsed-field-gradient spin-echo diffusion measurement. *Phys. Rev. B* 51, 15074–15078. doi:10.1103/PhysRevB.51.15074.
- Mollink, J., Kleinnijenhuis, M., Cappellen van Walsum, A. M. van, Sotiropoulos, S. N., Cottaar, M., Mirfin, C., et al. (2017). Evaluating fibre orientation dispersion in white matter: Comparison of diffusion MRI, histology and polarized light imaging. *Neuroimage* 157, 561–574. doi:10.1016/j.neuroimage.2017.06.001.
- Mori, S., and Zhang, J. (2006). Principles of Diffusion Tensor Imaging and Its Applications to Basic Neuroscience Research. *Neuron* 51, 527–539. doi:10.1016/j.neuron.2006.08.012.
- Morozov, D., Bar, L., Sochen, N., and Cohen, Y. (2015). Microstructural information from angular double-pulsed-field-gradient NMR: From model systems to nerves. *Magn. Reson. Med.* 74, 25–32. doi:10.1002/mrm.25371.
- Nilsson, M., Lätt, J., Ståhlberg, F., van Westen, D., and Hagslätt, H. (2012). The importance of axonal undulation in diffusion MR measurements: A Monte Carlo simulation study. *NMR Biomed.* 25, 795–805. doi:10.1002/nbm.1795.
- Nørhøj Jespersen, S., and Buhl, N. (2011). The displacement correlation tensor: Microstructure, ensemble anisotropy and curving fibers. *J. Magn. Reson.* 208, 34–43. doi:10.1016/j.jmr.2010.10.003.
- Novikov, D. S., Fieremans, E., Jensen, J. H., and Helpert, J. A. (2011). Random walks with barriers. *Nat. Phys.* 7, 508–514. doi:10.1038/nphys1936.
- Nunes, D., Cruz, T. L., Jespersen, S. N., and Shemesh, N. (2017). Mapping axonal density and average diameter using non-monotonic time-dependent gradient-echo MRI. *J. Magn. Reson.* 277, 117–130. doi:10.1016/j.jmr.2017.02.017.
- Özarslan, E. (2009). Compartment shape anisotropy (CSA) revealed by double pulsed field gradient MR. *J. Magn. Reson.* 199, 56–67. doi:10.1016/j.jmr.2009.04.002.

- Palombo, M., Ligneul, C., Najac, C., Le Douce, J., Flament, J., Escartin, C., et al. (2016a). New paradigm to assess brain cell morphology by diffusion-weighted MR spectroscopy in vivo. *Proc. Natl. Acad. Sci.* 113, 6671–6676. doi:10.1073/pnas.1504327113.
- Palombo, M., Ligneul, C., Najac, C., Le Douce, J., Flament, J., Escartin, C., et al. (2016b). New paradigm to assess brain cell morphology by diffusion-weighted MR spectroscopy in vivo. *Proc. Natl. Acad. Sci.* 113, 201504327. doi:10.1073/pnas.1504327113.
- Palombo, M., Shemesh, N., Ronen, I., and Valette, J. (2017). Insights into brain microstructure from in vivo DW-MRS. *Neuroimage*. doi:10.1016/j.neuroimage.2017.11.028.
- Panagiotaki, E., Schneider, T., Siow, B., Hall, M. G., Lythgoe, M. F., and Alexander, D. C. (2012). Compartment models of the diffusion MR signal in brain white matter: A taxonomy and comparison. *Neuroimage* 59, 2241–2254. doi:10.1016/j.neuroimage.2011.09.081.
- Papaioannou, A., Novikov, D. S., Fieremans, E., and Boutis, G. S. (2017). Observation of structural universality in disordered systems using bulk diffusion measurement. *Phys. Rev. E* 96, 61101. doi:10.1103/PhysRevE.96.061101.
- Prasloski, T., Mädler, B., Xiang, Q. S., MacKay, A., and Jones, C. (2012). Applications of stimulated echo correction to multicomponent T2analysis. *Magn. Reson. Med.* 67, 1803–1814. doi:10.1002/mrm.23157.
- Reisert, M., Kellner, E., Dhital, B., Hennig, J., and Kiselev, V. G. (2017). Disentangling micro from mesostructure by diffusion MRI: A Bayesian approach. *Neuroimage* 147, 964–975. doi:10.1016/j.neuroimage.2016.09.058.
- Reynaud, O., Winters, K. V., Hoang, D. M., Wadghiri, Y. Z., Novikov, D. S., and Kim, S. G. (2016). Surface-to-volume ratio mapping of tumor microstructure using oscillating gradient diffusion weighted imaging. *Magn. Reson. Med.* 76, 237–247. doi:10.1002/mrm.25865.
- Schwartz, E. D., Cooper, E. T., Chin, C.-L., Wehrli, S., Tessler, A., and Hackney, D. B. (2005). Ex vivo evaluation of ADC values within spinal cord white matter tracts. *AJNR. Am. J. Neuroradiol.* 26, 390–397.
- Shemesh, N., Adiri, T., and Cohen, Y. (2011). Probing microscopic architecture of opaque heterogeneous systems using double-pulsed-field-gradient NMR. *J. Am. Chem. Soc.* 133, 6028–6035.
- Shemesh, N., Barazany, D., Sadan, O., Bar, L., Zur, Y., Barhum, Y., et al. (2012a). Mapping apparent eccentricity and residual ensemble anisotropy in the gray matter using angular double-pulsed-field-gradient MRI. *Magn. Reson. Med.* 68. doi:10.1002/mrm.23300.
- Shemesh, N., and Cohen, Y. (2011a). Microscopic and compartment shape anisotropies in gray and white matter revealed by angular bipolar double-PFG MR. *Magn. Reson. Med.* 65, 1216–1227.
- Shemesh, N., and Cohen, Y. (2011b). Overcoming apparent Susceptibility-Induced Anisotropy (aSIA) by bipolar double-Pulsed-Field-Gradient NMR. *J. Magn. Reson.* 212, 362–369.
- Shemesh, N., Jespersen, S. N., Alexander, D. C., Cohen, Y., Drobnjak, I., Dyrby, T. B., et al. (2016). Conventions and nomenclature for double diffusion encoding NMR and MRI. *Magn. Reson. Med.* 75. doi:10.1002/mrm.25901.
- Shemesh, N., Özarslan, E., Adiri, T., Bassar, P. J., and Cohen, Y. (2010a). Noninvasive bipolar double-pulsed-field-gradient NMR reveals signatures for pore size and shape in polydisperse, randomly oriented, inhomogeneous porous media. *J. Chem. Phys.* 133.
- Shemesh, N., Özarslan, E., Bassar, P. J., and Cohen, Y. (2009). Measuring small compartmental dimensions with low-q angular double-PGSE NMR: The effect of experimental parameters on signal decay. *J. Magn. Reson.* 198, 15–23.

- Shemesh, N., Özarslan, E., Basser, P. J., and Cohen, Y. (2010b). Detecting diffusion-diffraction patterns in size distribution phantoms using double-pulsed field gradient NMR: Theory and experiments. *J. Chem. Phys.* 132.
- Shemesh, N., Rosenberg, J. T., Dumez, J.-N., Grant, S. C., and Frydman, L. (2017). Distinguishing neuronal from astrocytic subcellular microstructures using in vivo Double Diffusion Encoded  $^1\text{H}$  MRS at 21.1 T. *PLoS One* 12. doi:10.1371/journal.pone.0185232.
- Shemesh, N., Rosenberg, J. T., Dumez, J.-N., Muniz, J. A., Grant, S. C., and Frydman, L. (2014a). Metabolic properties in stroked rats revealed by relaxation-enhanced magnetic resonance spectroscopy at ultrahigh fields. *Nat. Commun.* 5. doi:10.1038/ncomms5958.
- Shemesh, N., Rosenberg, J. T., Dumez, J. N., Muniz, J. A., Grant, S. C., and Frydman, L. (2014b). Metabolic properties in stroked rats revealed by relaxation-enhanced magnetic resonance spectroscopy at ultrahigh fields. *Nat. Commun.* 5, 1–8. doi:10.1038/ncomms5958.
- Shemesh, N., Westin, C. F., and Cohen, Y. (2012b). Magnetic resonance imaging by synergistic diffusion-diffraction patterns. *Phys. Rev. Lett.* 108.
- Stejskal, E.O., Tanner, J. E. (1965). Spin Diffusion Measurements: Spin Echoes in the Presence of a Time-Dependent Field. *J. Chem. Phys.* 42, 288–292.
- Stepišnik, J. (1993). Time-dependent self-diffusion by NMR spin-echo. *Phys. B Phys. Condens. Matter* 183, 343–350. doi:10.1016/0921-4526(93)90124-O.
- Stepišnik, J., Lasič, S., Mohorič, A., Serša, I., and Sepe, A. (2006). Spectral characterization of diffusion in porous media by the modulated gradient spin echo with CPMG sequence. *J. Magn. Reson.* 182, 195–199. doi:10.1016/j.jmr.2006.06.023.
- Szczepankiewicz, F., Lasič, S., van Westen, D., Sundgren, P. C., Englund, E., Westin, C. F., et al. (2015). Quantification of microscopic diffusion anisotropy disentangles effects of orientation dispersion from microstructure: Applications in healthy volunteers and in brain tumors. *Neuroimage* 104, 241–252. doi:10.1016/j.neuroimage.2014.09.057.
- Ulloa, P., Wotschel, V., and Koch, M. A. (2015). Studying the extracellular contribution to the double wave vector diffusion-weighted signal. *Curr. Dir. Biomed. Eng.* 1, 240–244. doi:10.1515/cdbme-2015-0060.
- Valette, J., Ligneul, C., Marchadour, C., Najac, C., and Palombo, M. (2018). Brain metabolite diffusion from ultra-short to ultra-long time scales: What do we learn, where should we go? *Front. Neurosci.* 12, 1–6. doi:10.3389/fnins.2018.00002.
- Vellmer, S., Edelhoff, D., Suter, D., and Maximov, I. I. (2017a). Anisotropic diffusion phantoms based on microcapillaries. *J. Magn. Reson.* 279, 1–10. doi:10.1016/j.jmr.2017.04.002.
- Vellmer, S., Stirnberg, R., Edelhoff, D., Suter, D., Stöcker, T., and Maximov, I. I. (2017b). Comparative analysis of isotropic diffusion weighted imaging sequences. *J. Magn. Reson.* 275, 137–147. doi:10.1016/j.jmr.2016.12.011.
- Veraart, J., Fieremans, E., and Novikov, D. S. (2016a). Universal power-law scaling of water diffusion in human brain defines what we see with MRI. 1–8. Available at: <http://arxiv.org/abs/1609.09145>.
- Veraart, J., Novikov, D. S., Christiaens, D., Ades-aron, B., Sijbers, J., and Fieremans, E. (2016b). Denoising of diffusion MRI using random matrix theory. *Neuroimage*, 1–28. doi:10.1016/j.neuroimage.2016.08.016.
- Wedeer, V. J., Hagmann, P., Tseng, W. Y. I., Reese, T. G., and Weisskoff, R. M. (2005). Mapping complex tissue architecture with diffusion spectrum magnetic resonance imaging. *Magn. Reson. Med.* 54, 1377–1386. doi:10.1002/mrm.20642.

- West, K. L., Kelm, N. D., Carson, R. P., and Does, M. D. (2016). A revised model for estimating g-ratio from MRI. *Neuroimage* 125, 1155–1158. doi:10.1016/j.neuroimage.2015.08.017.
- Westin, C. F., Knutsson, H., Pasternak, O., Szczepankiewicz, F., Özarslan, E., van Westen, D., et al. (2016). Q-space trajectory imaging for multidimensional diffusion MRI of the human brain. *Neuroimage* 135, 345–362. doi:10.1016/j.neuroimage.2016.02.039.
- Wilhelm, M. J., Ong, H. H., Wehrli, S. L., Li, C., Tsai, P.-H., Hackney, D. B., et al. (2012). Direct magnetic resonance detection of myelin and prospects for quantitative imaging of myelin density. *Proc. Natl. Acad. Sci.* 109, 9605–9610. doi:10.1073/pnas.1115107109.
- Xu, J., Does, M. D., and Gore, J. C. (2009). Quantitative characterization of tissue microstructure with temporal diffusion spectroscopy. *J. Magn. Reson.* 200, 189–197. doi:10.1016/j.jmr.2009.06.022.
- Xu, J., Li, H., Harkins, K. D., Jiang, X., Xie, J., Kang, H., et al. (2014). Mapping mean axon diameter and axonal volume fraction by MRI using temporal diffusion spectroscopy. *Neuroimage* 103, 10–19. doi:10.1016/j.neuroimage.2014.09.006.
- Xu, J., Li, K., Smith, R. A., Waterton, J. C., Zhao, P., Chen, H., et al. (2012). Characterizing tumor response to chemotherapy at various length scales using temporal diffusion spectroscopy. *PLoS One* 7. doi:10.1371/journal.pone.0041714.
- Zatorre, R. J., Fields, R. D., and Johansen-Berg, H. (2012). Plasticity in gray and white: Neuroimaging changes in brain structure during learning. *Nat. Neurosci.* 15, 528–536. doi:10.1038/nn.3045.

## Tables

**Table 1.** White Matter and Gray Matter microscopic and fractional anisotropies, along with their Spearman correlation coefficient and significance.

	$\mu$ FA DODE	FA DODE	Spearman's $\rho$	p-value	$\mu$ FA DDE	FA DDE	Spearman's $\rho$	p-value
<b>White Matter</b>			0.41	$<10^{-10}$			0.19	$<10^{-10}$
Mean	0.77	0.49			0.89	0.69		
$\sigma$	0.10	0.12			0.16	0.13		
<b>Gray Matter</b>			0.22	$<10^{-10}$			-0.10	$<0.002$
Mean	0.71	0.24			0.79	0.31		
$\sigma$	0.10	0.15			0.10	0.18		

**Table 2.** Statistical analysis of correlations between ( $\mu$ )FA and myelin water fraction in white matter and gray matter.

	$\mu$ FA DODE	FA DODE	$\mu$ FA DDE	FA DDE
<b>White Matter</b>				
Spearman's $\rho$	-0.36	0.02	-0.07	0.30
p-value	$<10^{-10}$	NS	0.0011	$<10^{-10}$
<b>Gray Matter</b>				
Spearman's $\rho$	0.23	0.11	0.45	-0.1
p-value	$<10^{-10}$	0.0002	$<10^{-10}$	0.0015

**Table 3.** Statistical analysis of correlations between ( $\mu$ )FA and literature-based average axon diameter (extracted from Dula et al) in the rat spinal cord.

	$\mu$ FA DODE	FA DODE	$\mu$ FA DDE	FA DDE
<b>White Matter</b>				
Spearman's $\rho$	-0.96	-0.68	-0.14	-0.43
p-value	0.0028	NS	NS	NS